Supporting Information for

Relationships between Greenland Ice Sheet melt season surface speeds and modeled effective pressures

Laura A. Stevens[1,2], Ian J. Hewitt[3], Sarah B. Das[4], and Mark D. Behn[4]

[1]Massachusetts Institute of Technology/Woods Hole Oceanographic Institution Joint Program in Oceanography/Applied Ocean Science and Engineering, Woods Hole, MA 02543, USA
[2]now at Lamont-Doherty Earth Observatory, Columbia University, Palisades, NY 10964, USA
[3]Mathematical Institute, University of Oxford, Oxford, UK
[4]Department of Geology and Geophysics, Woods Hole Oceanographic Institution, Woods Hole, MA, USA

Contents of this file:

Text S1. Subglacial Hydrology Model Governing Equations

The subglacial water flow model is the two-dimensional model of the subglacial drainage system used by *Banwell et al.* [2016] and originally developed by *Hewitt* [2013]. The model routes ice sheet surface meltwater input into a continuous "sheet" connected to discrete "channels" melted upwards into the base of the ice sheet [*Hewitt*, 2013]. A schematic of model parameters is given in Fig. 2. Water moves between the continuous sheet of some average thickness h, and flux, $\boldsymbol{q_s}$ (vector quantity); channels of cross-sectional area S and discharge Q; and englacial storage Σ, to maintain a continuous hydraulic potential ϕ given by

$$\phi = \rho_w g b + p_w, \tag{S.1}$$

where ρ_w is the water density, g is the gravitational acceleration, b is the basal elevation, and p_w is the water pressure. Water flux in the sheet $\boldsymbol{q_s}$ is dependent on sheet thickness h, through

$$\boldsymbol{q_s} = -\frac{K_s h^3}{\rho_w g} \nabla \phi, \tag{S.2}$$

where K_s is the sheet flux coefficient controlling the sheet permeability, making $K_s h^3$an effective hydraulic transmisivity.

Water in the sheet is further divided into two components: a cavity sheet of thickness h_{cav} and an elastic sheet of thickness h_{el}. The sum of the height of the cavity and elastic sheet is equal to total sheet thickness: $h = h_{cav} + h_{el}$. The thickness of the cavity sheet represents the height of water-filled cavities [*Creyts and Schoof*, 2009; *Schoof et al.*, 2012], and is a balance between the combined effects of basal ice melt and basal sliding opening cavities, and ice creep closing cavities according to

$$\frac{\partial h_{cav}}{\partial t} = \frac{\rho_w}{\rho_i} m + \frac{U_b (h_r - h_{cav})}{l_r} - \frac{2A}{n^n} h_{cav} |N|^{n-1} N, \tag{S.3}$$

where ρ_i is the ice density, m is the basal melting rate, U_b is the basal sliding speed, h_r is the bed roughness height scale, l_r is the bed roughness length scale, A is the creep parameter in Glen's law, n is the creep exponent in Glen's law, and N is the effective pressure ($N = p_i - p_w$). The magnitude of basal sliding speed U_b (scalar quantity) is prescribed everywhere to be 100 m yr^{-1}, which is not ideal as winter surface ice velocities in the region range from ~50–250 m yr^{-1} (Fig. 1c) and exhibit variability in speedup during the melt season (Fig. 1e) [*Joughin et al.*, 2013]. The fixed value of U_b is not ideal, as it results in a fixed rate of subglacial cavity opening (Eq. S.3). However, as most of the water flux is accommodated by channels during the melt season, a fixed U_b likely has minimal effect on model output.

Basal melting rate in the sheet, m, is prescribed everywhere to be 0.0059 m yr^{-1} based on an average geothermal heat flux, G, beneath Greenland of 0.063 W m^{-2} [*Rogozhina et al.*, 2012] according to the equation

$$m = \frac{G}{\rho_w L}, \tag{S.4}$$

where L is the latent heat of melting.

The elastic sheet is included to represent the elastic uplift or "hydraulic jacking" of ice where $p_w > p_i$. Here h_{el} is related to effective pressure, $N = p_i - p_w$, through

$$h_{el} = \begin{cases} -C_{el}\left(N - \frac{1}{2}N_0\right), & N < 0 \\ C_{el}\frac{(N_0 - N)^2}{2N_0}, & 0 < N < N_0 \\ 0, & N > N_0 \end{cases} \tag{S.5}$$

where C_{el} is the uplift compliance and N_0 is a small regularizing pressure used to smooth this relationship. Based on this form, h_{el} is zero when N is positive ($p_i > p_w$), but increases rapidly when p_w approaches or exceeds p_i ($N \leq 0$). A constant value for C_{el} of 1.02×10^{-6} m Pa^{-1} is set for all model runs, resulting in 1 m of uplift for 100 m of excess hydraulic head (There is a typo in the value of C_{el} in *Banwell et al.* [2016].). While this treatment of h_{el} allows for the injection of a large amount of meltwater into the subglacial drainage system without generating unrealistically large water pressures in the cavity layer or channels, elastic bending stress in the ice is not accounted for. For example, a non-zero h_{el} at one node does not necessarily cause its neighboring nodes to also become hydraulically jacked. Rather, the activation of the elastic sheet affects the pressure gradient between neighboring nodes. As stated above, the sum of the height of the cavity and elastic sheet is the total sheet thickness, which drives discharge in the sheet (Eq. S.2).

Water in the sheet is connected to discrete channels. Water discharge in the channels, Q, is given by

$$Q = -K_c S^{\frac{5}{4}} \left|\frac{\partial \phi}{\partial s}\right|^{-\frac{1}{2}} \frac{\partial \phi}{\partial s}, \tag{S.6}$$

where K_c is a turbulent flow coefficient for channel flow, and S is the cross-sectional area of channel at a distance along the channel s. The growth and decay of channel cross-sectional area is a competition between the melt back and creep closure of channel walls given by

$$\frac{\partial S}{\partial t} = \frac{\rho_w}{\rho_i} M - \frac{2A}{n^n} S|N|^{n-1}N, \tag{S.7}$$

where M is the melting rate. The melting rate M, is expressed as

$$M = \frac{\left|Q\frac{\partial \phi}{\partial s}\right|}{\rho_w L} + \frac{\lambda_c |\boldsymbol{q} \cdot \nabla \phi|}{\rho_w L}, \tag{S.8}$$

where λ_c is the incipient sheet width contributing to channel melting (the length scale over which ice melting contributes to channel formation). The first term is the channel melting rate as a function of channel discharge and hydraulic potential along the channel, and the second term should be viewed as a parameterization of how small channels emerge from a sheet flow [*Hewitt et al.*, 2012]. The appropriate value for λ_c is rather uncertain and discussed in Section 4.4.1.

Finally, mass conservation is expressed as a balance between the sheet, channels, and englacial storage with basal melting, channel wall melting, and surface runoff inputs R according to

$$\left[\frac{\partial h}{\partial t} + \nabla \cdot \boldsymbol{q_s}\right] + \left[\frac{\partial S}{\partial t} + \frac{\partial Q}{\partial s}\right]\delta(x_c) + \frac{\partial \Sigma}{\partial t} = m + M\delta(x_c) + R, \qquad \text{(S.9)}$$

where Σ is englacial storage, which represents the additional water storage in connected englacial void space [*Harper et al.*, 2010; *Bartholomaus et al.*, 2011; *Hewitt*, 2013]. Englacial storage is related to water pressure through

$$\Sigma = \sigma \frac{p_w}{\rho_w g} + A_m \frac{p_w}{\rho_w g}\, \delta(x_m), \qquad \text{(S.10)}$$

where σ is the connected void fraction of the ice and A_m is the cross-sectional area of the moulin. For Eqs. S.9 and S.10, the delta functions only apply at the line positions of the channels, $x_c(s)$, and the point positions of moulins, x_m.

Text S2. Numerical procedure

The subglacial hydrology equations above are discretized onto a two-dimensional, regular rectangular mesh and solved using a finite difference approach [*Hewitt*, 2013]. Nodes are spaced 900-m apart. The continuous variables hydraulic potential ϕ, water sheet thickness h, and water pressure p_w are discretized onto the nodes of the grid. Every node on the grid is the center of a finite volume square over which flux in the sheet, $\boldsymbol{q_s}$, is calculated. Eight potential channels connect every node to its closest surrounding eight nodes. Moulins are defined on a selection of the nodes x_m chosen based on the surface runoff forcing as discussed in Section 4.3.2.4. The non-linear system for the evolution of p_w, h, and S described in Eqs. (S.1–S.10) is solved at each timestep using an iterative Newton method with variable time step length based on the success of the last iteration. The maximum time step the model can take is set to one day, with time steps decreasing to only a couple hours during periods of high surface runoff during the melt season.

Text S3. Coherence and spectral estimation.

We employ coherence estimates to compare goodness of fit between surface speeds, static variables, and model output effective pressures. Coherence is a bivariate statistic in the spectral domain that is analogous to correlation in the spatial domain [*Simons et al.*, 2000]. Coherence measures the phase relationship between two signals, with high coherence values indicating constructive interference at wavenumbers where the two signals are correlated [for review, see *Kirby*, 2014]. For geophysical problems, one-dimensional coherence was first used by *Forsyth* [1985] to estimate flexural rigidity of the lithosphere through coherence between topography and gravity anomalies along transects across continental rift valleys [*Forsyth*, 1985]. The approach was expanded by *Simons et al.* [2000] to investigate two-dimensional lithospheric loading from the coherence between two-dimensional fields of topography and gravity anomalies [*Simons et al.*, 2000, 2003]. The coherence estimation between two two-dimensional fields yields information in the spectral, spatial, and azimuthal domains, which provides the wavelength, spatial, and directional dependence of the coherence between the two fields, respectively [*Simons et al.*, 2003].

We follow the methodology and analysis routines of *Simons et al.* [2000] for estimating two-dimensional coherence of stationary fields. For two stochastic fields (*e.g.,* surface ice velocity (X) and bedrock topography (Y)) defined on $\boldsymbol{d}$ in the spatial domain and $\boldsymbol{k}$ in the Fourier domain, the coherence-square function between the two fields, γ_{XY}^2, is the ratio between the magnitude of the fields' cross-spectral density, S_{XY}, and the power spectral density of the individual fields, S_{XX} and S_{YY}:

$$\gamma_{XY}^2(\boldsymbol{d},\boldsymbol{k}) = \frac{|S_{XY}(\boldsymbol{d},\boldsymbol{k})|^2}{S_{XX}(\boldsymbol{d},\boldsymbol{k})S_{YY}(\boldsymbol{d},\boldsymbol{k})}. \tag{S.11}$$

Like correlation estimates, coherence-square estimates range from $0 < \gamma_{XY}^2 < 1$, with $\gamma_{XY}^2 = 1$ indicating an entirely consistent phase relationship between both fields [*Simons et al.*, 2003].

Some amount of averaging in the wavenumber domain must be completed prior to calculating γ_{XY}^2 to prevent the ratio of periodograms expressed in Eq. S.11 from always yielding $\gamma_{XY}^2 = 1$ [*Bendat and Piersol*, 1993]. Following *Simons et al.* [2000], we use multitaper spectral estimation [*Thomson*, 1982] with two-dimensional Slepian tapers [*Slepian*, 1978] on a Cartesian plane to perform this wavenumber averaging. A weighted average of the spectra is created by multiplying the data by a set of several chosen tapers, taking the two-dimensional Fourier transform of these data-taper products, and finally taking a average in wavenumber space of the resulting power spectra [*Kirby*, 2014]. The result is a coherence-square estimation over the wavenumber domain, $\gamma_{XY}^2(\boldsymbol{k_X},\boldsymbol{k_Y})$. Isotropic coherence-square estimates, $\gamma^2(|\boldsymbol{k}|)$, are calculated by averaging over 360° of azimuth around logarithmically-spaced annuli in the wavenumber domain [*Kirby*, 2014]. A coherence-square estimation of synthetic data is provided in Figure S4 to illustrate this methodology.

The number and bandwidth of the chosen set of tapers determines the wavenumber resolution and variance of the coherence-square estimate [*Simons et al.*, 2000]. A higher number of tapers and/or a wider taper bandwidth reduces the variance in the coherence-square estimate and reduces the waveband resolution [*Kirby*, 2014]. Most studies choose taper bandwidths to be the width of 2–5 wavenumber bands [*Simons et al.*, 2000; *Kirby*, 2014]. For this study, we set the taper bandwidth, NW, to 3 and the number of tapers K to 4 for all coherence-square estimates.

As the coherence-square estimate is a statistic, the variance of the isotropic coherence-square estimate is calculated following the Cramer-Rao lower bound:

$$\sigma^2\{\gamma^2(|\boldsymbol{k}|)\} = \frac{2\gamma^2\frac{(1-\gamma^2)^2}{J}}{\Lambda}, \tag{S.12}$$

which is a measurement of variance determined by maximum likelihood estimates [*Seymour and Cumming*, 1994; *Simons et al.*, 2003], where J is the number of uncorrelated spectral estimators over which the coherence-square estimate is made [*Simons et al.*, 2003], and Λ is the number of points in the wavenumber annuli [*Simons et al.*, 2000]. In our two-dimensional case, $J = K^2$ [*Simons et al.*, 2003]. As we have set $K = 4$, $J = K^2 = 16$ uncorrelated spectral estimators. Error estimates of $\gamma^2(|\boldsymbol{k}|)$ presented throughout the paper are two standard deviations, 2σ. With $J = 16$, the 2σ values across all possible $\gamma^2(|\boldsymbol{k}|)$ values increases with increasing wavelength, from a minimum of 0.025 at 2 km wavelength to maximum of 0.96 at 30.9 km wavelength.

Finally, the range of wavelengths we can investigate in the spectral domain is set by our data length, (N_X, N_Y), and data spacing, (dx, dy), in the spatial domain. Our coherence-square estimates are constrained by surface velocity data from single-look complex TerraSAR-X radar images, which have $dx = dy = 0.1\ km$, $N_X = 309$ data points, and $N_Y = 552$ data points. The longest resolvable wavelength (the Rayleigh wavelength, λ_R) is set by the shorter x dimension to be $\lambda_{RX} = N_X dx = 30.9\ km$. The shortest resolvable wavelength in either direction is the Nyquist wavelength, $\lambda_N = 2\ dx = 0.2\ km$.

Table S1: Values and ranges used for model parameters.

ρ_w	Water density	1000 kg m^{-3}
ρ_i	Ice density	910 kg m^{-3}
g	Gravitational acceleration	9.8 m s^{-2}
A	Glen's law fluidity coefficient	6.8×10^{-24} Pa^{-3} s^{-1}
n	Glen's law exponent	3
L	Latent heat of melting	3.5×10^{5} J kg^{-3}
G	Greenland geothermal heat flux	0.063 W m^{-2} **
σ	Englacial void fraction	[10^{-4}, 10^{-3}, 10^{-2}]
K_c	Turbulent flow coefficient for channel flow	0.1 m s^{-1} Pa$^{-1/2}$
K_s	Sheet flux coefficient (sheet permeability)	[10^{-4}, 10^{-3}, 10^{-2}] m^{-1} s^{-1} *
λ_c	Sheet width contributing to melting	[100; 1000; 5000] m *
c	Specific heat capacity of water	4200 J kg^{-1} K^{-1}
β	Melting point pressure gradient	7.8×10^{-8} K Pa^{-1}
h_r	Bed roughness height scale	0.1 m
l_r	Bed roughness length scale	10 m
U_b	Basal sliding speed	100 m yr^{-1}
C_{el}	Uplift regularization rate	1.02×10^{-6} m Pa^{-1}
A_m	Moulin cross-sectional area	10 m^{2}

* range of values that differs from *Banwell et al.* (2016)
** value from *Rogozhina et al.* [2012]

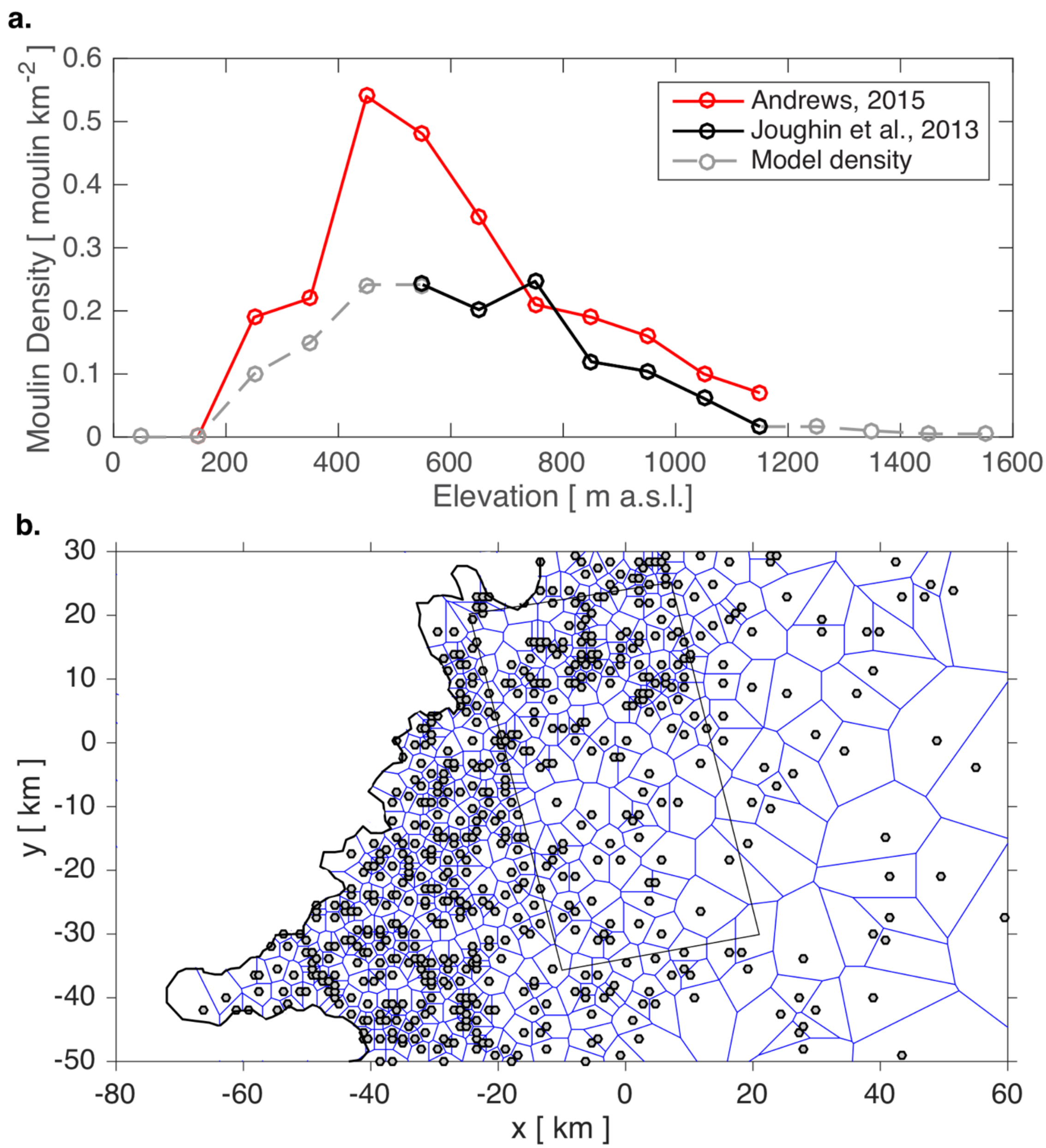

Figure S1. Moulin density and discrete surface runoff catchment delineation. (**a**) Moulin density versus elevation from *Joughin et al.* [2013] map (black), the Paakitsoq region (red) (from *Andrews* [2015]), and the model domain (grey). (**b**) Voronoi cells calculated for discrete moulin locations $\boldsymbol{x_m}$ (grey circles).

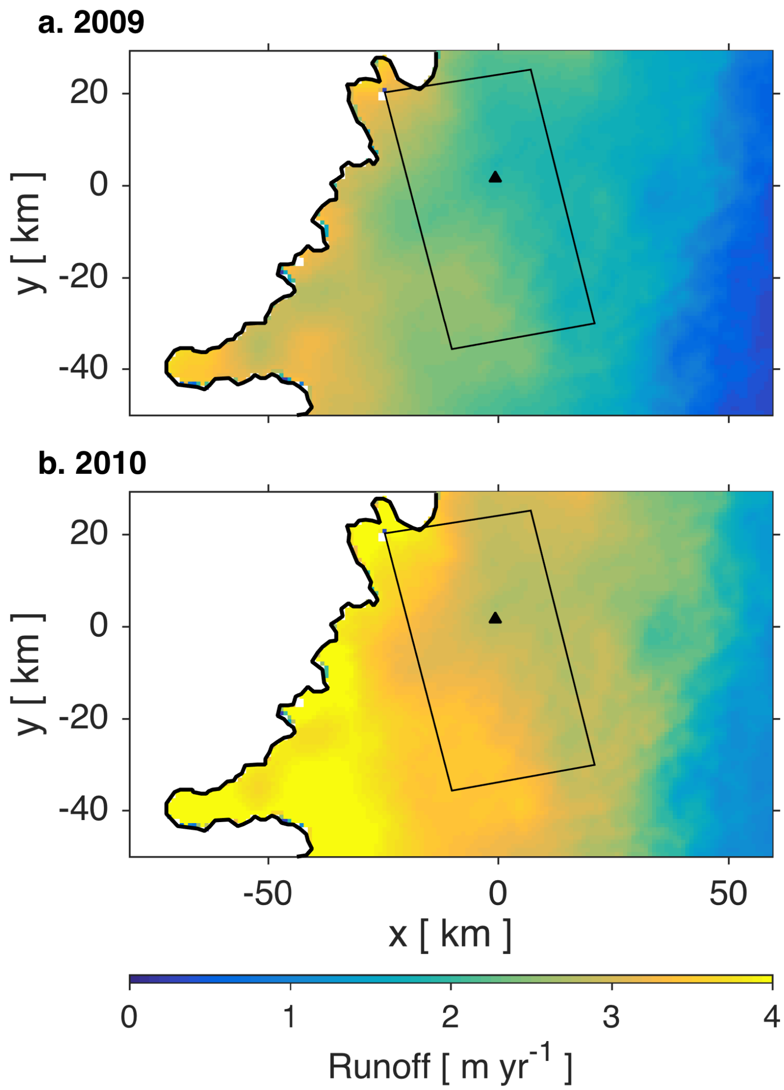

Figure S2. Total runoff across the model domain in (a) **2009 and** (b) **2010.**

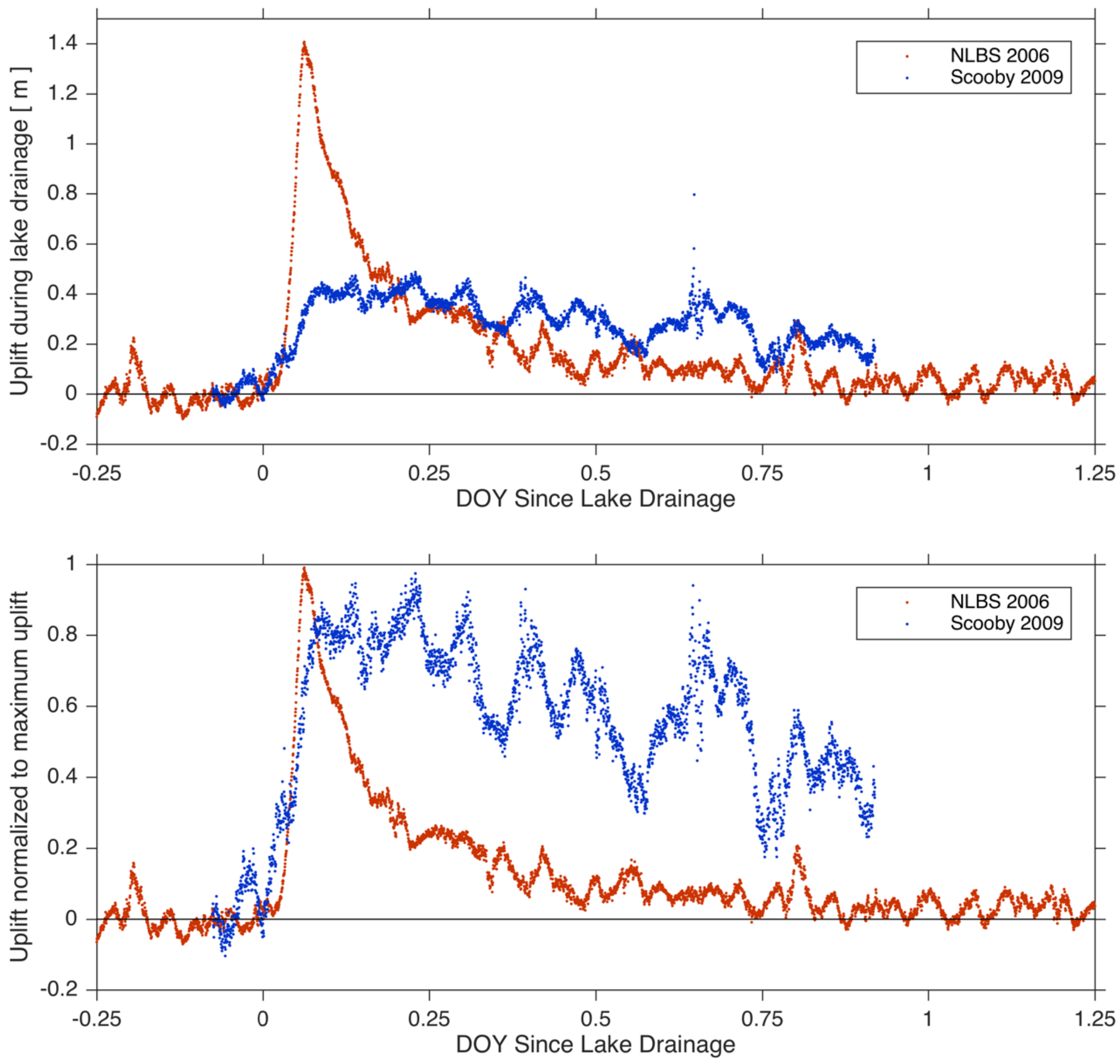

Figure S3: Surface ice displacement during the rapid drainage of North Lake on 2006 DOY 210 and 2009 DOY 168. (**a**) Uplift of NLBS GPS station in 2006 (red) and "Scooby" GPS station in 2009 (blue) during North Lake rapid drainage events. Both stations are located at 68.74˚ N 49.50˚ W, roughly 1.5 km north of the lake margin. (**b**) Uplift of the same two stations normalized to their maximum uplift during respective North Lake rapid drainage events.

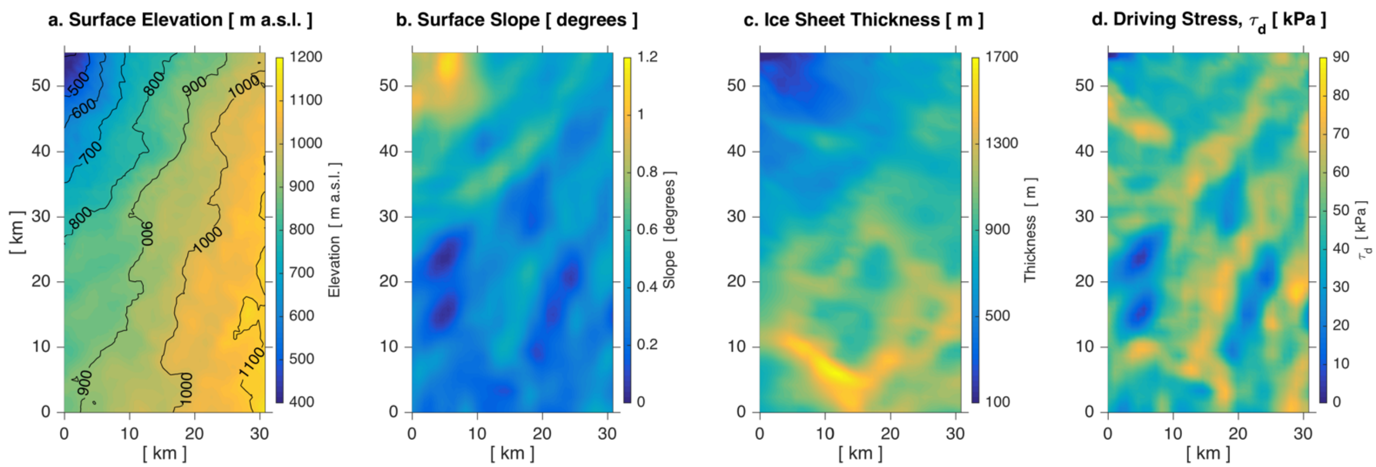

Figure S4: Surface elevation, surface slope, ice sheet thickness, and driving stress τ_d for the TerraSAR-X region.

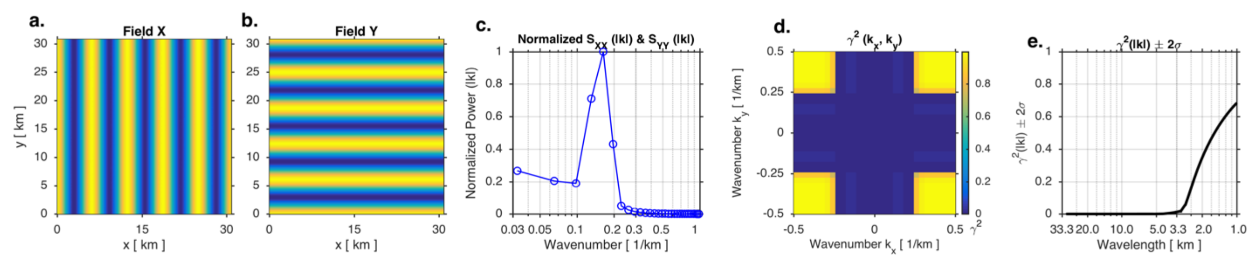

Figure S5. Coherence-square estimation of synthetic data. 2-dimensional, 6-km wavelength sine wave along the (**a**) x-axis and (**b**) y-axis. **c**) Isotropically averaged power of the two fields' power spectral densities, $\boldsymbol{S_{XX}}$ and $\boldsymbol{S_{YY}}$, plotted by wavenumber. Power is plotted normalized to the maximum value in each fields' isotropically averaged power. Power for each field peaks at $0.1\overline{6}$ wavenumber, which is at 6-km wavelength (wavenumber = 1/wavelength). **d**) The coherence-square estimates between fields X **(a)** and Y **(b)** in wavenumber space, $\gamma^2(\boldsymbol{k_X}, \boldsymbol{k_Y})$, where the smallest wavenumbers (largest, Rayleigh wavelengths) plot in the center of plot ($\boldsymbol{k_X} = \lambda_R$, $\boldsymbol{k_Y} = \lambda_R$), and the largest wavenumbers (smallest, Nyquist wavelengths) plot at the edges of the plot. The scale for the $\boldsymbol{k_X}$ and $\boldsymbol{k_Y}$ axes are linear in wavenumber. Wavenumber axis is log scale. Zero coherence is observed along the $\boldsymbol{k_X}$ and $\boldsymbol{k_Y}$ axes where the two fields have destructive interference. Coherence between the two fields switches to 1 at wavenumbers above 0.25 and wavelengths smaller than 4 km. **e**) The isotropically averaged coherence-square estimate, $\gamma^2(|\boldsymbol{k}|) \pm 2\sigma$, between fields **a** and **b**. The log x-axis is equivalent to the axis in panel **c**, but x-axis tickmarks are now labeled in wavelength.

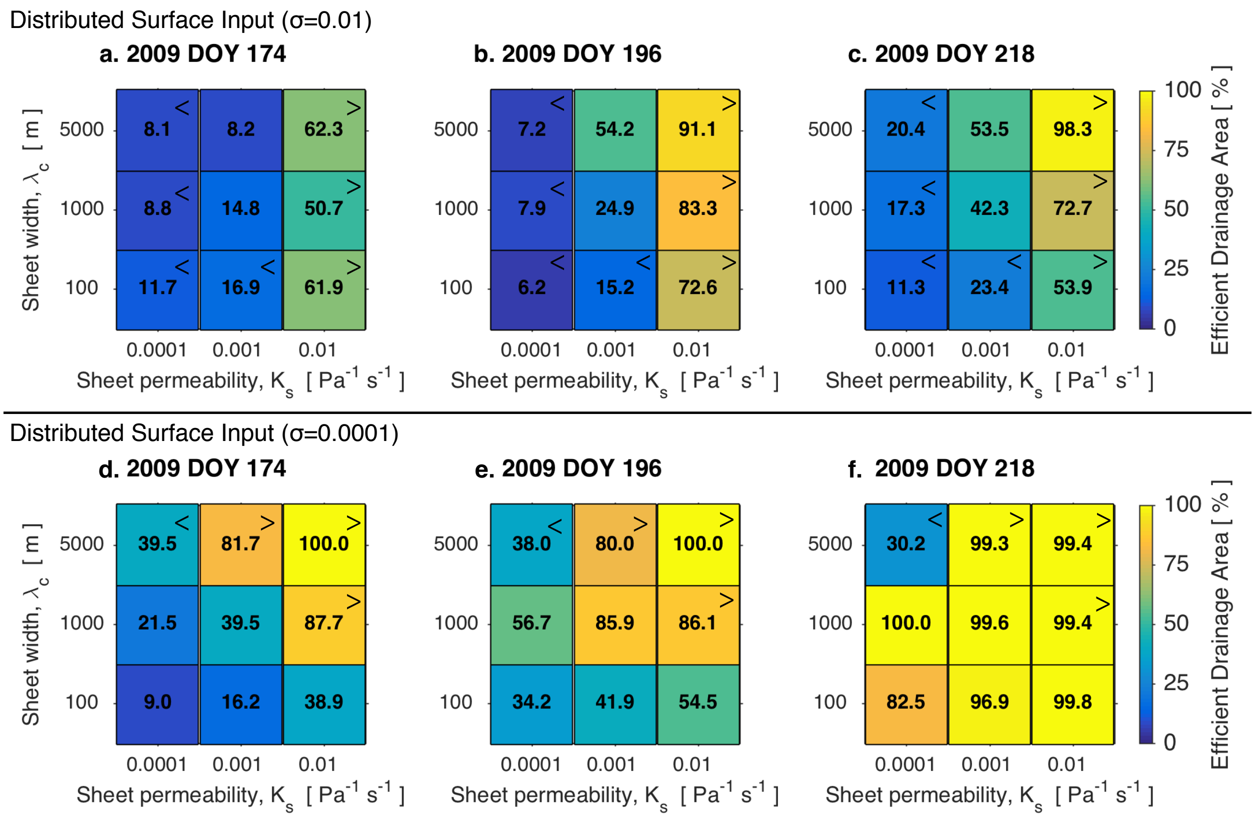

Figure S6. Region of efficient drainage area for 2009 distributed surface runoff input at $\boldsymbol{\sigma = 0.01}$ and $\boldsymbol{\sigma = 0.0001}$. Percentage of efficient drainage area across K_s and λ_c parameter space for distributed surface input models on DOY (**a**) 174, (**b**) 196, and (**c**) 218 of 2009 with $\sigma = 0.01$. Percentage of efficient drainage area across K_s and λ_c parameter space for distributed surface input models on DOY (**d**) 174, (**e**) 196, and (**f**) 218 of 2009 with $\sigma = 0.0001$. Efficient drainage area is defined as the area within the TerraSAR-X region where $N > 0$ and $q > 0.001$ m^2 s^{-1}. ">" mark models that channelize too quickly with an EDA > 40% on DOY 174 2009. "<" mark models that channelize too slowly with an EDA < 40% on DOY 218 2009.

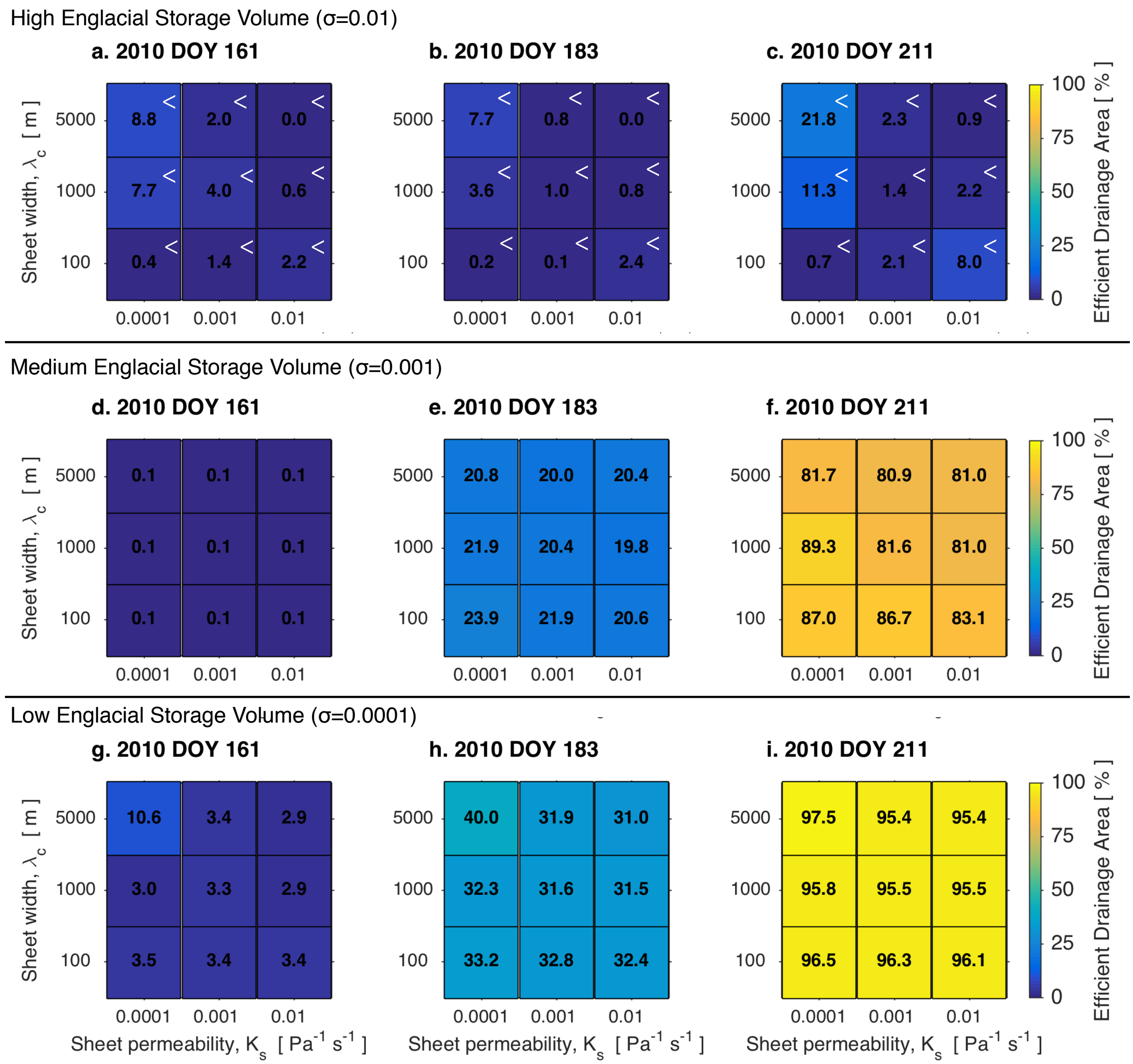

Figure S7. Region of efficient drainage area for 2010 distributed surface runoff input. Percentage of efficient drainage area across K_s and λ_c parameter space for distributed surface input models on DOY 161, 183, and 211 of 2010. Efficient drainage area (EDA) is defined as the area within the TerraSAR-X region where $N > 0$ and $q > 0.001$ m^2 s^{-1}. Englacial void fraction σ decreases down the three rows of the figure from $\sigma = 0.01$ (a–c), to $\sigma = 0.001$ (d–f), to $\sigma = 0.0001$ (g–i). "<" mark models that channelize too slowly with an EDA < 40% on DOY 211 2010.

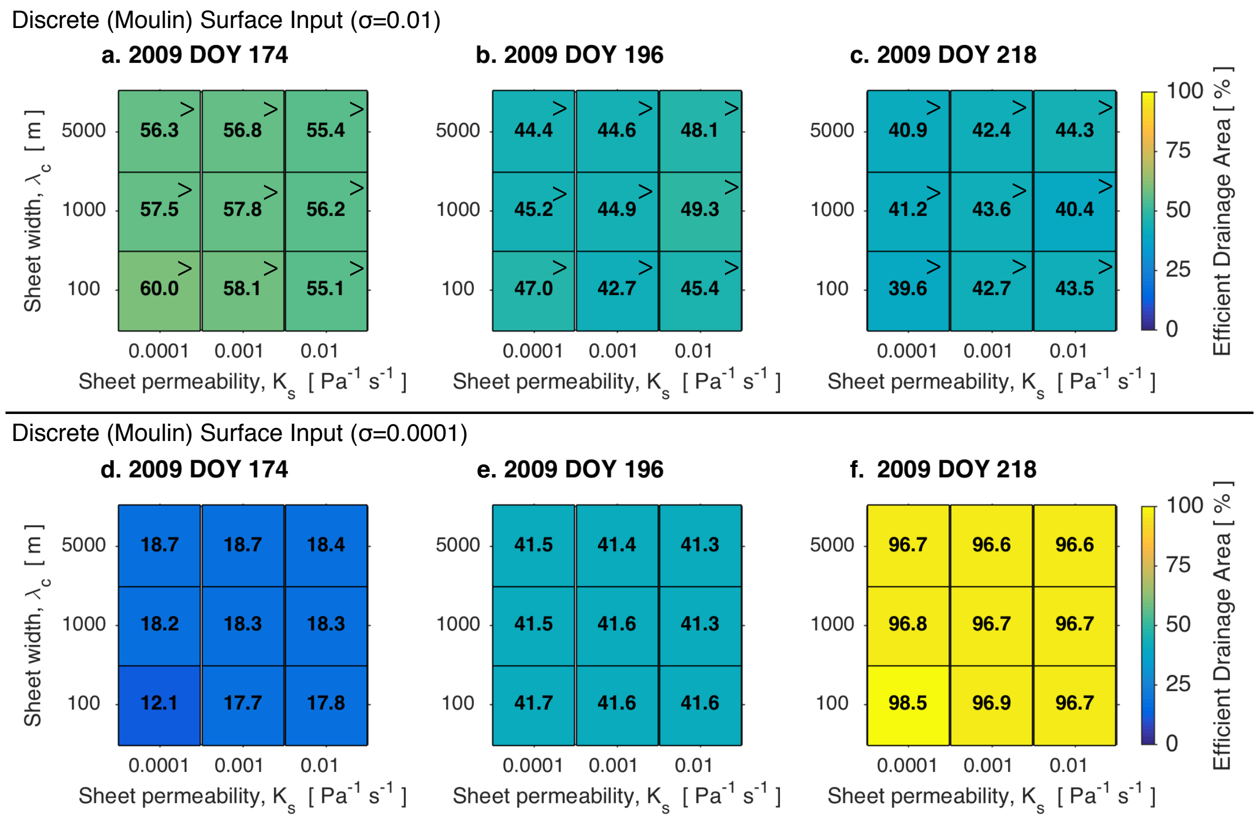

Figure S8. Region of efficient drainage area for 2009 discrete surface runoff input at $\sigma = 0.01$ and $\sigma = 0.0001$. Percentage of efficient drainage area across K_s and λ_c parameter space for discrete surface input models on DOY (**a**) 174, (**b**) 196, and (**c**) 218 of 2009 with $\sigma = 0.01$. Percentage of efficient drainage area across K_s and λ_c parameter space for discrete surface input models on DOY (**d**) 174, (**e**) 196, and (**f**) 218 of 2009 with $\sigma = 0.0001$. Efficient drainage area is defined as the area within the TerraSAR-X region where $N > 0$ and $q > 0.001$ m^2 s^{-1}. ">" mark models that channelize too quickly with an EDA > 40% on DOY 174 2009.

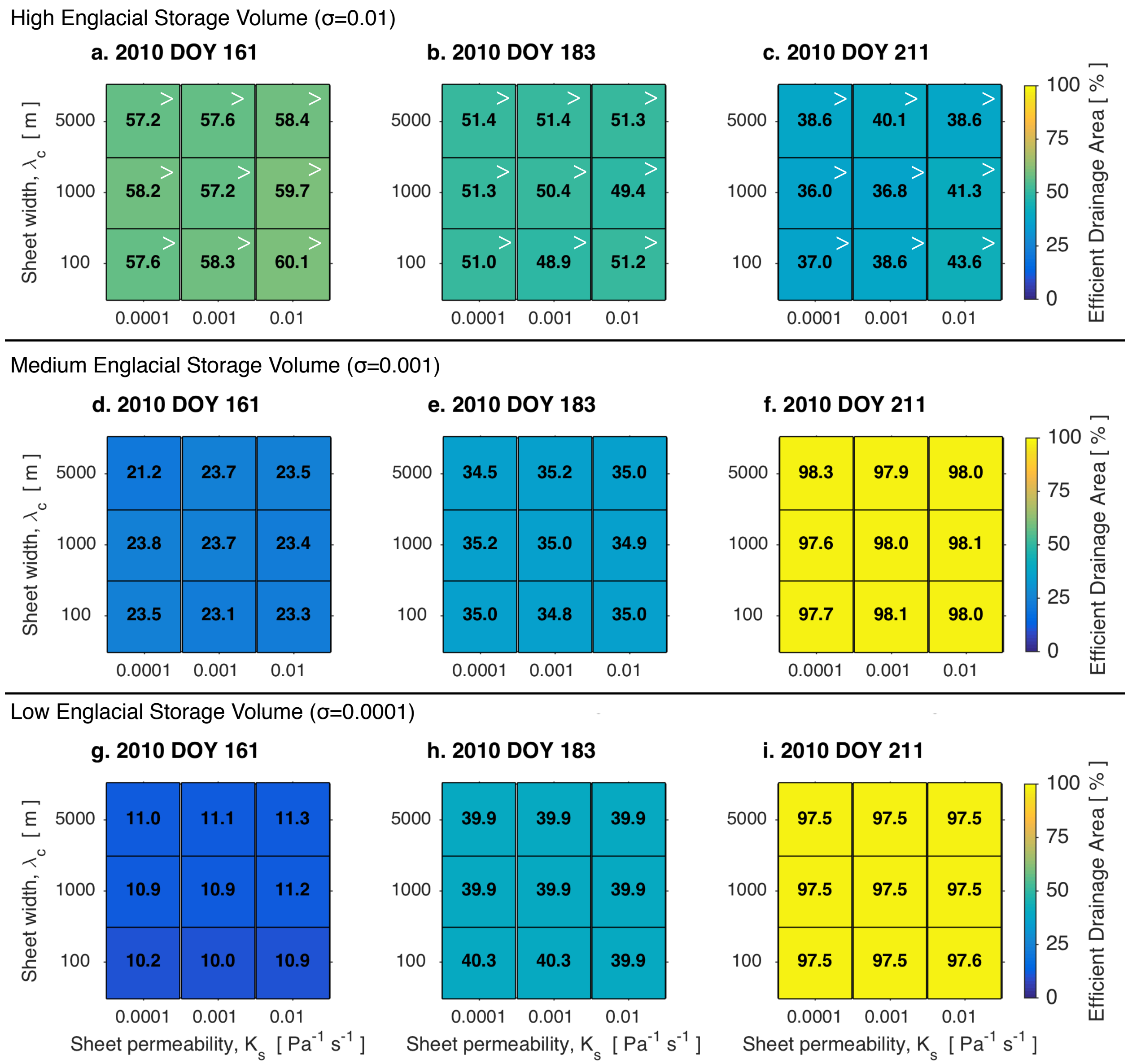

Figure S9. Region of efficient drainage area for 2010 discrete surface runoff input. Percentage of efficient drainage area across K_s and λ_c parameter space for discrete surface input models on DOY 161, 183, and 211 of 2010. Efficient drainage area (EDA) is defined as the area within the TerraSAR-X region where $N > 0$ and $q > 0.001$ m^2 s^{-1}. Englacial void fraction σ decreases down the three rows of the figure from $\sigma = 0.01$ (a–c), to $\sigma = 0.001$ (d–f), to $\sigma = 0.0001$ (g–i). “>” mark models that channelize too quickly with an EDA > 40% on DOY 161 2010.

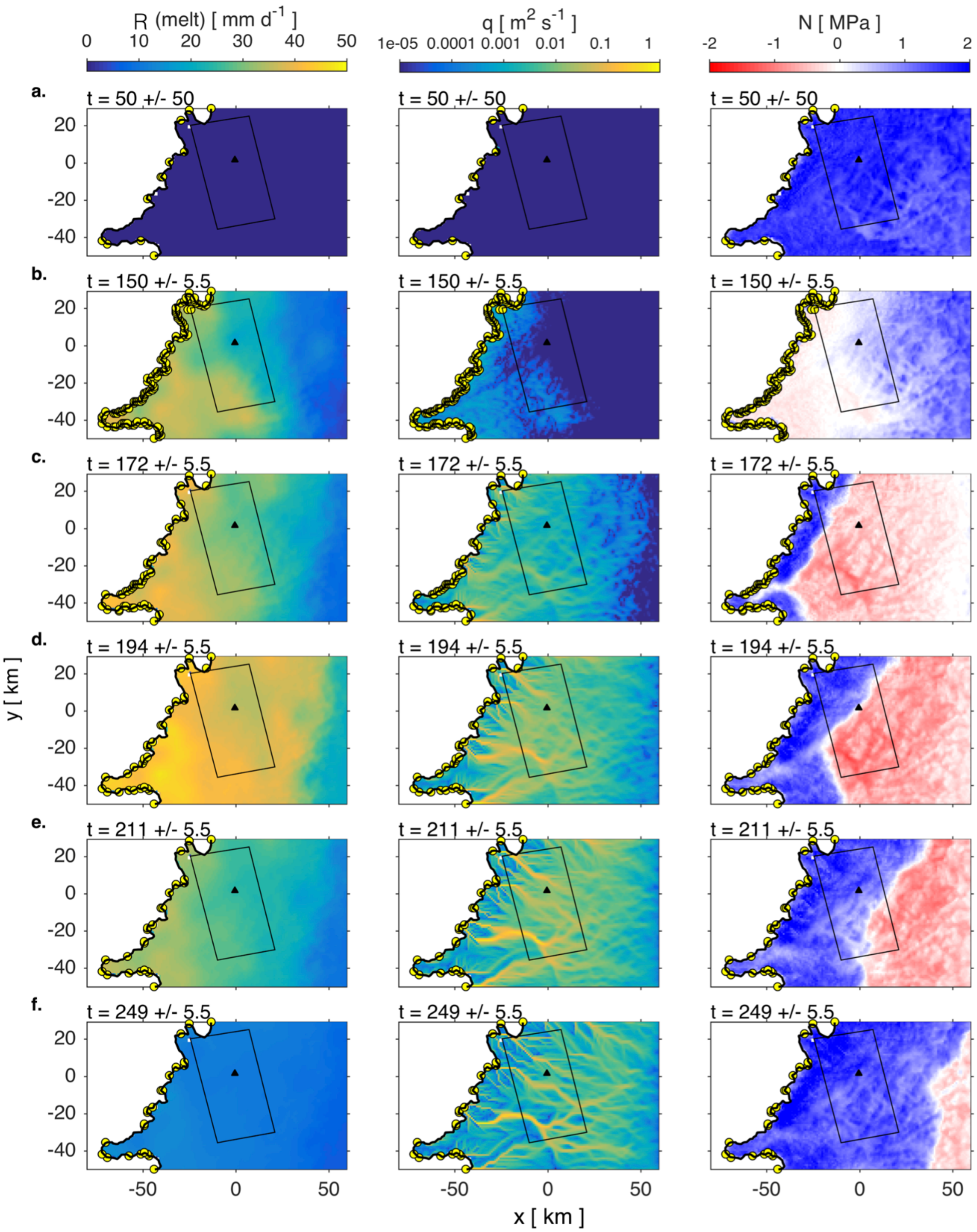

Figure S10. Averages of surface melt forcing, R (mm day^{-1}) (left column), subglacial water flux, q (m^2 s^{-1}) (middle column), and effective pressure, N (MPa) (right column) at each node over the 2010 melt season for a distributed surface input scenario. The date at the top of the panel corresponds to the central date for the interval over which the model outputs were determined. Parameters used in this model run are: $K_s = 0.001$ Pa^{-1} s^{-1}, $\sigma = 0.001$, and $\lambda_c = 1000\ m$. Black rectangle is the area outline of the ice flow maps in Figs. 1c-e. Black triangle marks the location of North Lake. Yellow circles mark discharge outlet locations along the ice sheet margin.

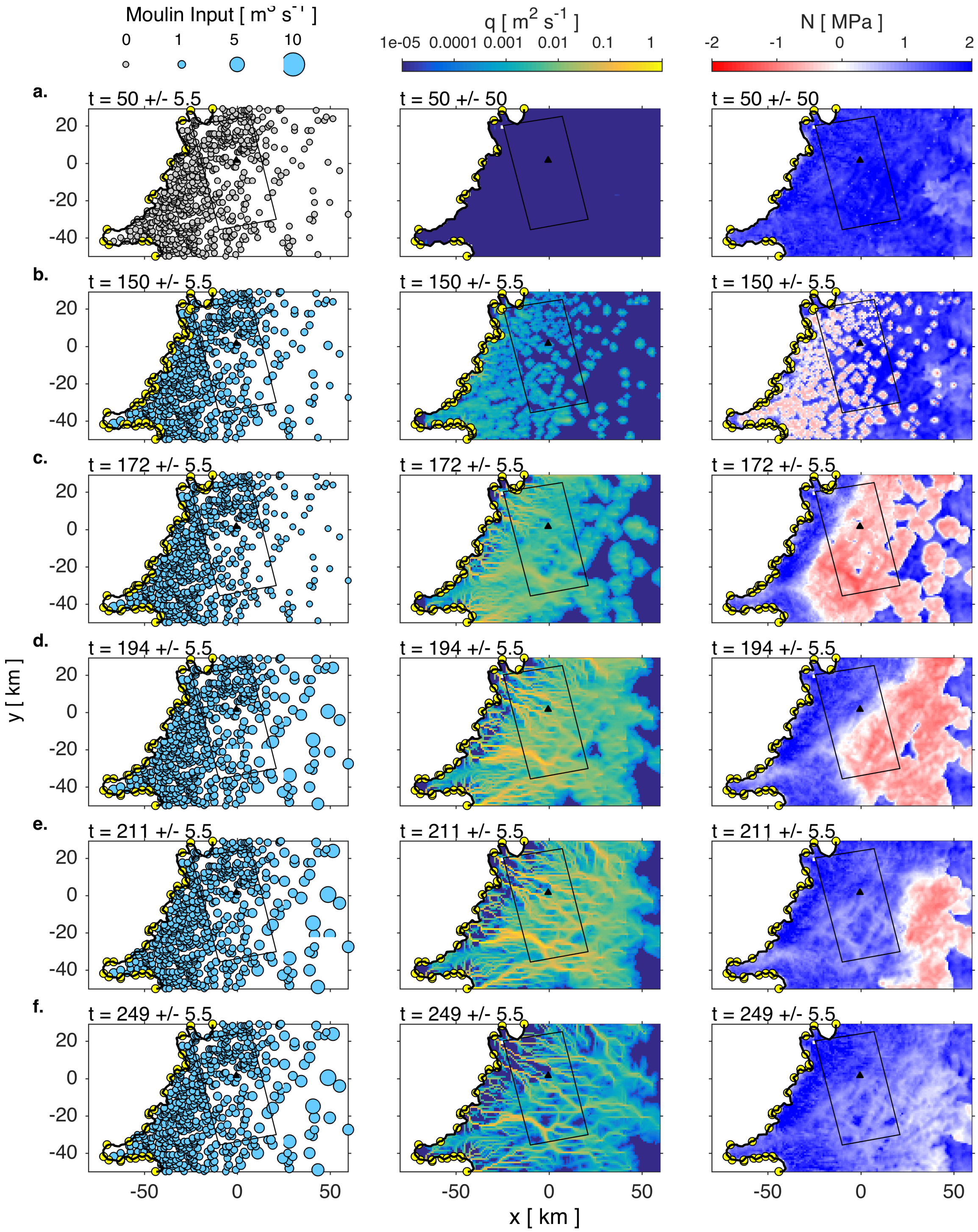

Figure S11. The same as Figure S9 but for a discrete surface input scenario in 2010. Left column is average moulin input (m^3 s^{-1}).

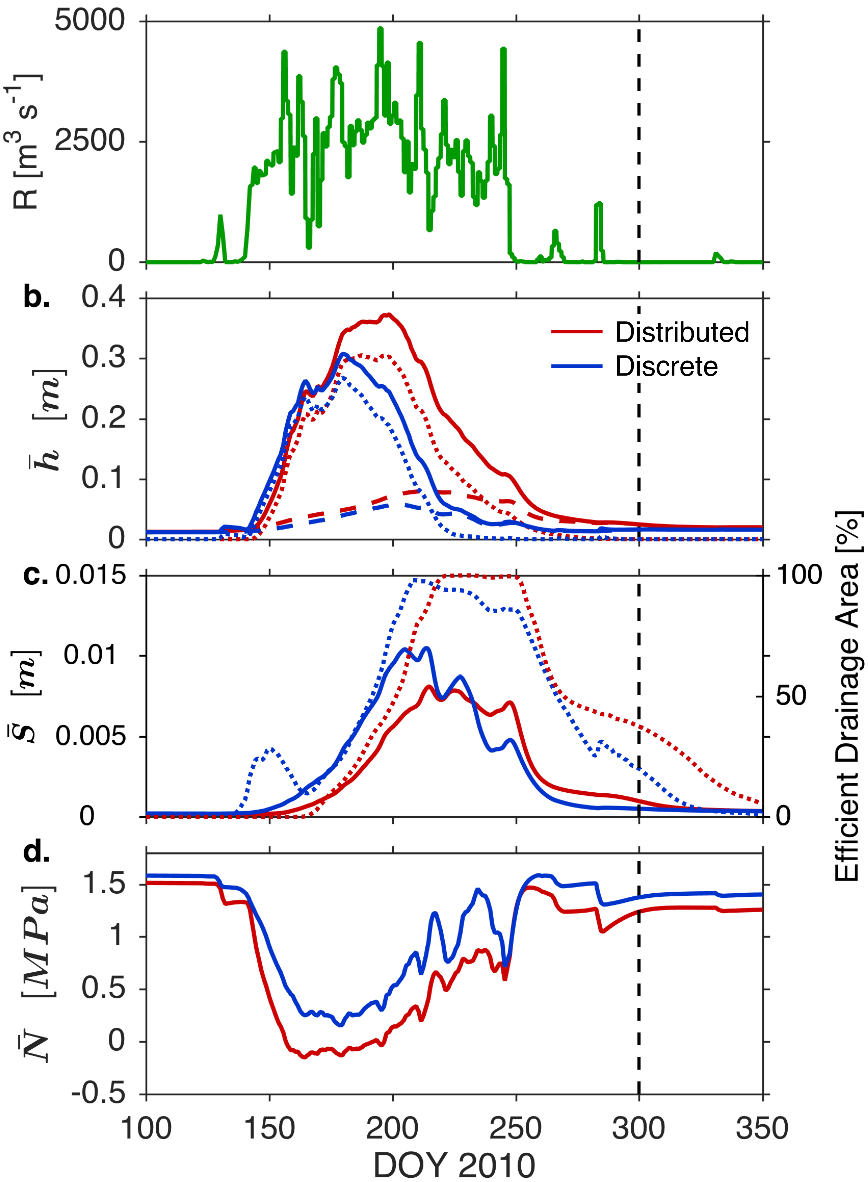

Figure S12. Differences in area-integrated model variables between the 2010 distributed (red) and discrete (blue) surface runoff input scenarios. (**a**) Surface runoff input integrated across the domain. (**b**) Average sheet height $\bar{h}$ across domain, with additional lines showing the contribution from the average cavity sheet height $\bar{h}_{cav}$ (dashed) the and average elastic sheet height $\bar{h}_{el}$ (dotted). (**c**) Average equivalent height of the channel layer $\bar{S}$ across the domain (solid lines) and the percentage of efficient drainage area of the TerraSAR-X region (dotted lines). Efficient drainage area (EDA) is defined as the area within the TerraSAR-X region where effective pressure $N > 0$ MPa and total flux $q > 0.001$ m^2 s^{-1}. (**d**) Area-averaged effective pressures N across the domain. Vertical dashed line through all plots marks the limit of the 2009 timeseries shown in Fig. 7.

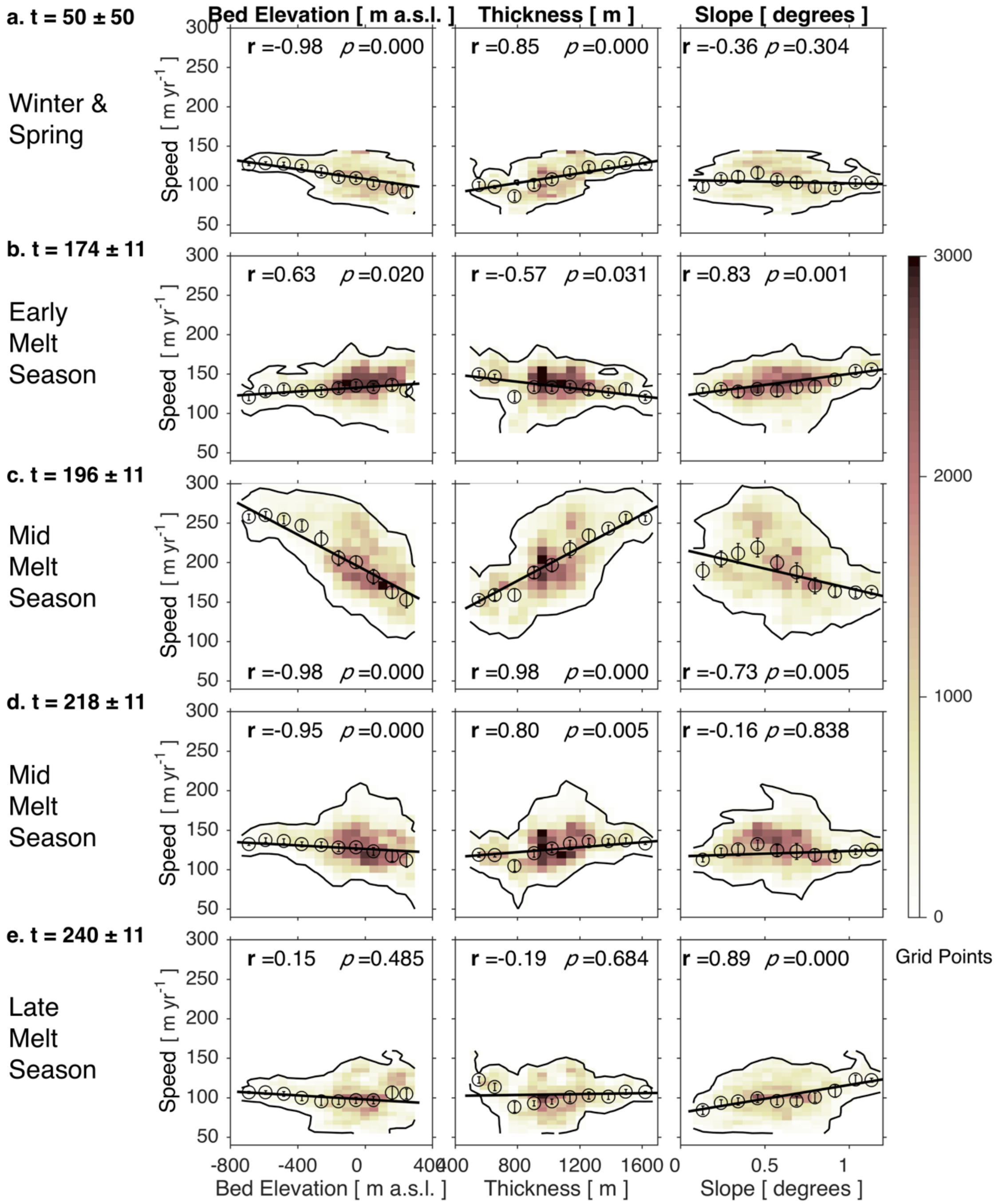

Figure S13. Correlations with bed elevation, ice sheet thickness, surface slope, and surface speeds through the 2009 melt season. Ice sheet thickness and surface slope against the winter RADARSAT and melt-season TerraSAR-X surface speed measurements. Data are linearly binned along the x- and y-axis, and the color of the bin represents the number of model grid points within that bin. Black contour surrounds data region with more than 10 model grid points. Surface speeds are averaged within each x-axis bin (circles), and are fit with a weighted linear regression (black line), where the y-value weights are 2 standard deviations (error bars). The weighted correlation coefficient **r** and the *p*-value are derived from the weighted linear regression.

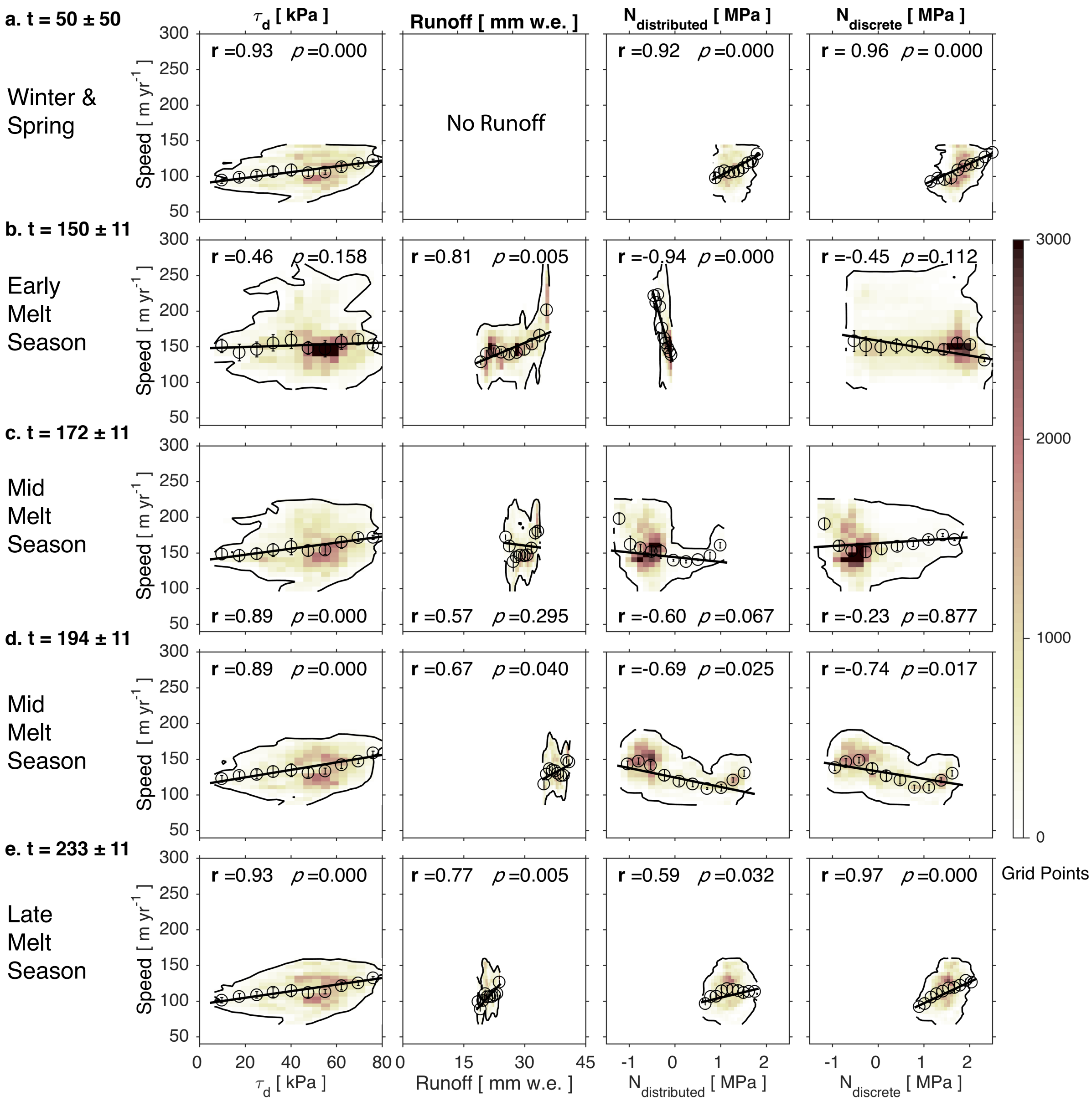

Figure S14. Correlations with surface speeds evolve through the 2010 melt season. Runoff, Driving stress τ_d, and model-derived 11-day averages of effective pressure *N* for a distributed and discrete input of surface forcing against the winter RADARSAT and melt-season TerraSAR-X surface speed measurements. Data are linearly binned along the x- and y-axis, and the color of the bin represents the number of model grid points within that bin. Black contour surrounds data region with more than 10 model grid points. Surface speeds are averaged within each x-axis bin (circles), and are fit with a weighted linear regression (black line), where the y-value weights are 2 standard deviations (error bars). The weighted correlation coefficient **r** and the *p*-value are derived from the weighted linear regression. Inset in effective pressure row **a** panels shows detail view of 50–150 m yr^{-1} winter surface speeds and 0–0.1 MPa effective pressures.

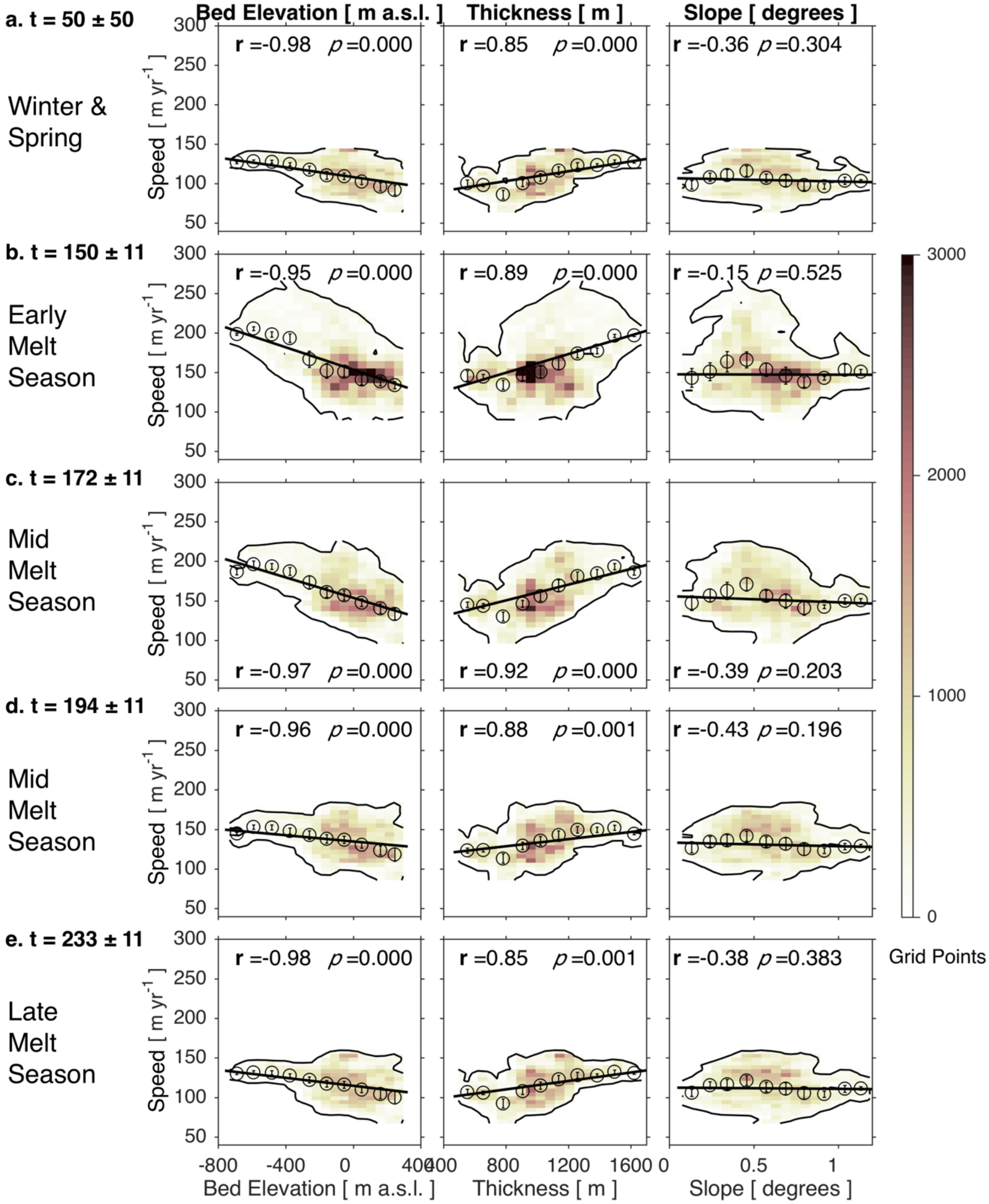

Figure S15. Correlations with bed elevation, ice sheet thickness, surface slope, and surface speeds through the 2010 melt season. Ice sheet thickness and surface slope against the winter RADARSAT and melt-season TerraSAR-X surface speed measurements. Data are linearly binned along the x- and y-axis, and the color of the bin represents the number of model grid points within that bin. Black contour surrounds data region with more than 10 model grid points. Surface speeds are averaged within each x-axis bin (circles), and are fit with a weighted linear regression (black line), where the y-value weights are 2 standard deviations (error bars). The weighted correlation coefficient **r** and the *p*-value are derived from the weighted linear regression.

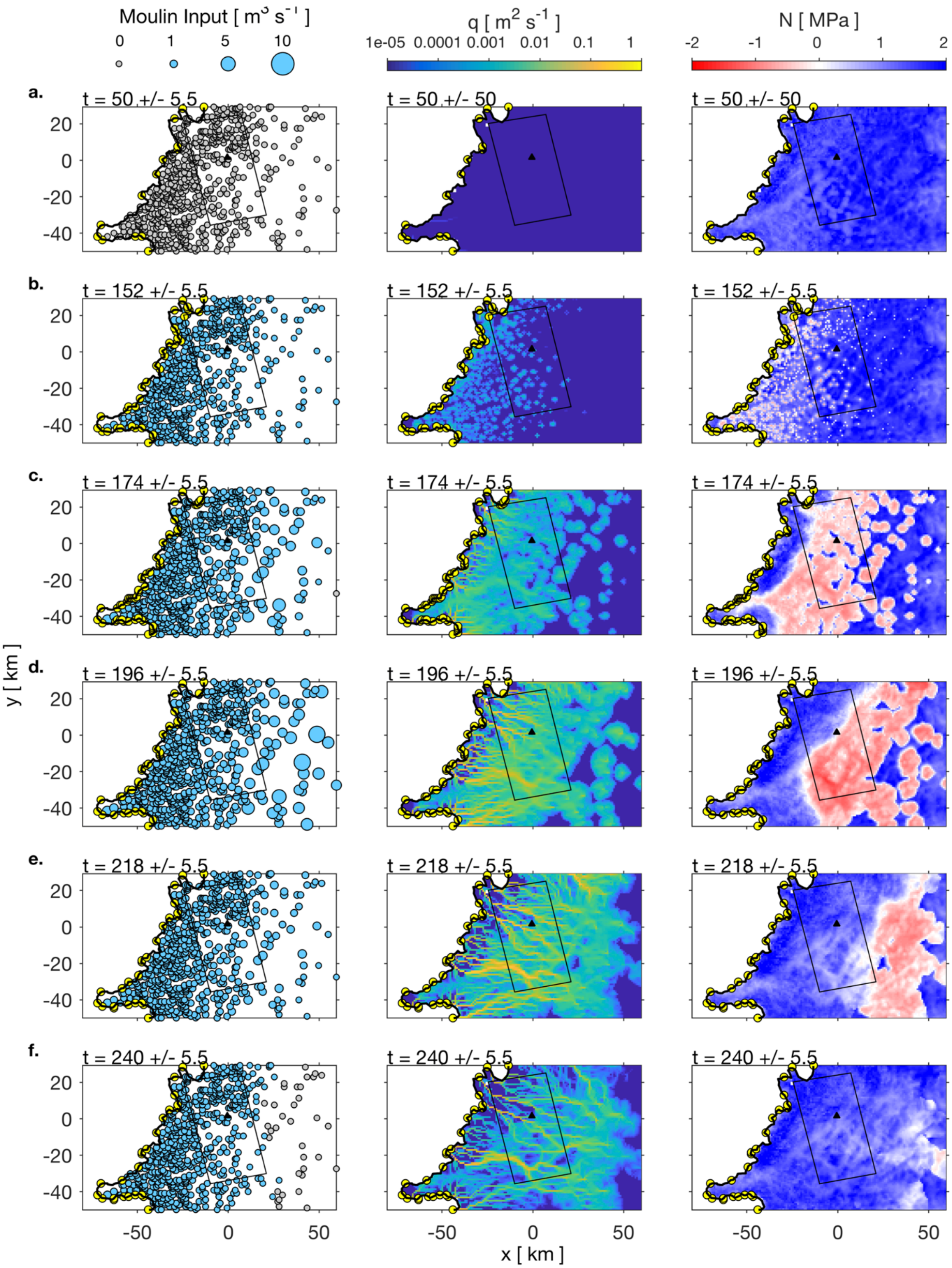

Figure S16. The same as Figure 4 but for a discrete surface input scenario with a pressure-dependent melting point. Left column is average moulin input (m^3 s^{-1}). Parameters used in this model run are: $K_s = 0.001$ Pa^{-1} s^{-1}, $\sigma = 0.001$, and $\lambda_c = 1000\ m$.

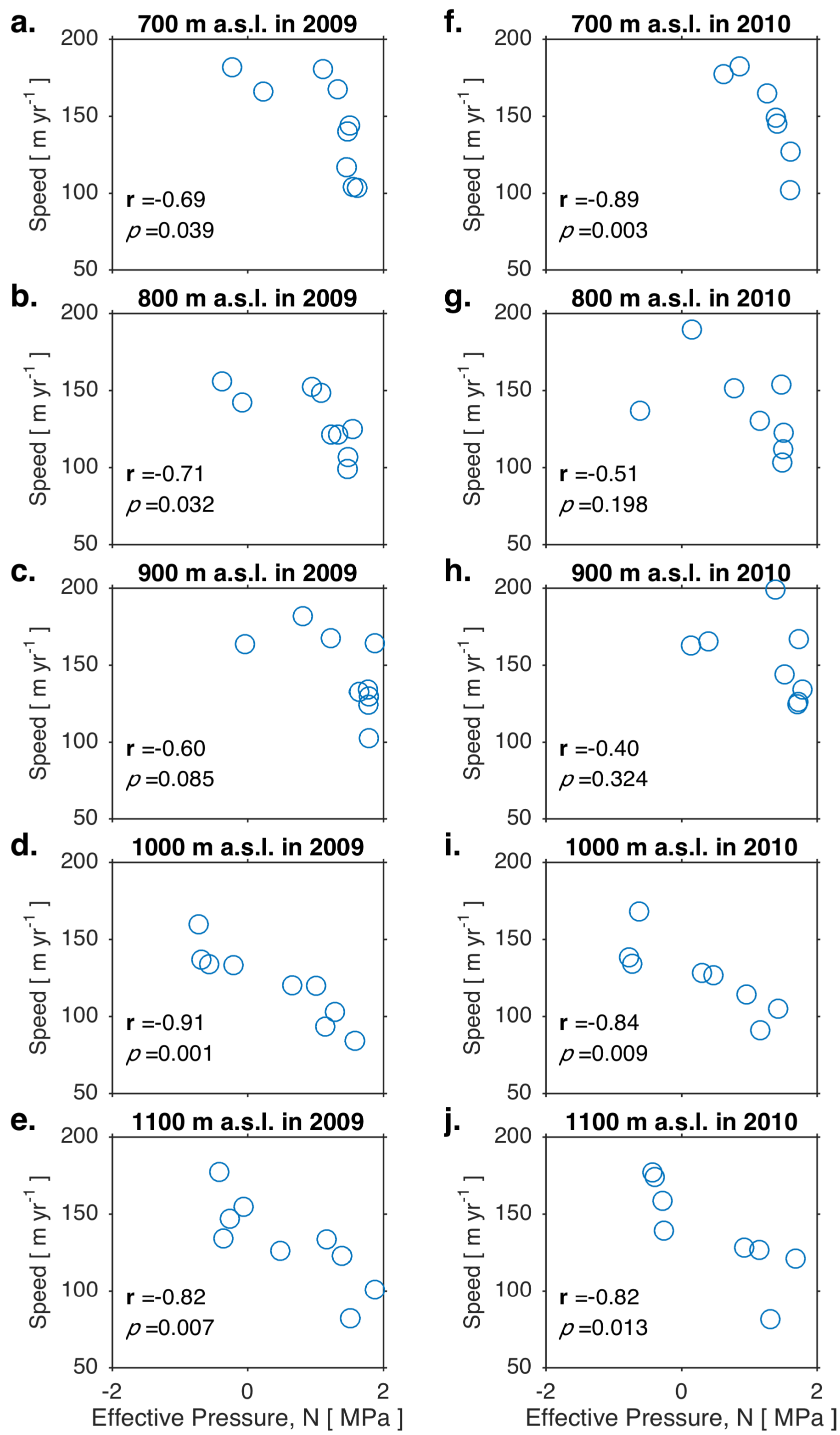

Figure S17. Scatter plot of 11-day averages of model-derived effective pressure N, versus 11-day TerraSAR-X speed observations for individual locations within the TerraSAR-X footprint. Locations are chosen at 100-m elevation contours from 700 m a.s.l. (**a**) to 1100 m a.s.l. (**e**). Left column depicts values for 2009 (**a–e**), and right column depicts values for 2010 (**f–i**). Average model-derived effective pressures are calculated from the models shown in Figure 5 (**a–e**, 2009) and Figure S11 (**f–i**, 2010).

References

Banwell, A., I. Hewitt, I. Willis, and N. Arnold (2016), Moulin density controls drainage development beneath the Greenland Ice Sheet, *J. Geophys. Res. Earth Surf.*, *121*, 2248–2269, doi:10.1002/2015JF003801.

Bartholomaus, T. C., R. S. Anderson, and S. P. Anderson (2011), Growth and collapse of the distributed subglacial hydrologic system of Kennicott Glacier , Alaska , USA , and its effects on basal motion, *J. Glaciol.*, *57*(206), 985–1002.

Bendat, J. S., and A. G. Piersol (1993), *Engineering Applications of Correlation and Spectral Analysis*, 2nd ed., John Wiley, New York.

Creyts, T. T., and C. G. Schoof (2009), Drainage through subglacial water sheets, *J. Geophys. Res. Earth Surf.*, *114*(4), 1–18, doi:10.1029/2008JF001215.

Forsyth, D. W. (1985), Subsurface loading and estimates of the flexural rigidity of continental lithosphere, *J. Geophys. Res. Planets*, *90*(B14), 12623–12632, doi:10.1029/JB090iB14p12623.

Harper, J. T., J. H. Bradford, N. F. Humphrey, and T. W. Meierbachtol (2010), Vertical extension of the subglacial drainage system into basal crevasses., *Nature*, *467*(7315), 579–582, doi:10.1038/nature09398.

Hewitt, I. J. (2013), Seasonal changes in ice sheet motion due to melt water lubrication, *Earth Planet. Sci. Lett.*, *371*, 16–25, doi:10.1016/j.epsl.2013.04.022.

Hewitt, I. J., C. Schoof, and M. A. Werder (2012), Flotation and free surface flow in a model for subglacial drainage. Part 2. Channel flow, *J. Fluid Mech.*, *702*, 157–187, doi:10.1017/jfm.2012.166.

Joughin, I., S. B. Das, G. E. Flowers, M. D. Behn, R. B. Alley, M. a. King, B. E. Smith, J. L. Bamber, M. R. van den Broeke, and J. H. van Angelen (2013), Influence of ice-sheet geometry and supraglacial lakes on seasonal ice-flow variability, *Cryosph.*, *7*(4), 1185–1192, doi:10.5194/tc-7-1185-2013.

Kirby, J. F. (2014), Estimation of the effective elastic thickness of the lithosphere using inverse spectral methods: The state of the art, *Tectonophysics*, *631*(C), 87–116, doi:10.1016/j.tecto.2014.04.021.

Rogozhina, I., J. M. Hagedoorn, Z. Martinec, K. Fleming, O. Soucek, R. Greve, and M. Thomas (2012), Effects of uncertainties in the geothermal heat flux distribution on the Greenland Ice Sheet: An assessment of existing heat flow models, *J. Geophys. Res.*, *117*, F02025, doi:10.1029/2011JF002098.

Schoof, C., I. J. Hewitt, and M. A. Werder (2012), Flotation and free surface flow in a model for subglacial drainage. Part 1. Distributed drainage, *J. Fluid Mech.*, *702*, 126–156, doi:10.1017/jfm.2012.165.

Seymour, M. S., and I. G. Cumming (1994), Maximum likelihood estimation for SAR interferometry, *Proc. Int. Geosci. Remote Sens. Symp.*, *4*, 2272–2275.

Simons, F. J., R. D. van der Hilst, and M. T. Zuber (2003), Spatiospectral localization of isostatic coherence anisotropy in Australia and its relation to seismic anisotropy: Implications for lithospheric deformation, *J. Geophys. Res. Earth*, *108*(B5), 2250, doi:10.1029/2001JB000704.

Simons, J., M. T. Zuber, and J. Korenaga (2000), Isostatic response of the Australian lithosphere: Estimation of effective elastic thickness and anisotropy using multitaper spectral analysis, *J. Geophys. Res.*, *105*(B8), 19163–19184.

Slepian, D. (1978), Prolate spheroidal wave functions, Fourier analysis, and uncertainty. V-The discrete case, *ATT Tech. J.*, *57*(5), 1371–1430, doi:10.1002/j.1538-7305.1978.tb02104.x.

Thomson, D. J. (1982), Spectrum estimation and harmonic analysis, *Proceeding Ieee*, *70*, 1055–1096.